The effect of hydrogen addition on the amplitude and harmonic response of azimuthal instabilities in a pressurized annular combustor

Thomas Indlekofer [a],*, Byeonguk Ahn [a], Yi Hao Kwah [a], Samuel Wiseman [a], Marek Mazur [b], James R. Dawson [a], Nicholas A. Worth [a]

[a] Department of Energy and Process Engineering, Norwegian University of Science and Technology, Trondheim N-7491, Norway
[b] CORIA-UMR 6641 Normandie Universit, CNRS-Universit et INSA de Rouen, Campus Universitaire du Madrillet, Saint Etienne du Rouvray, France

ABSTRACT

The present work introduces an annular combustion chamber operated at intermediate pressures. The combustor is operated with CH_4-H_2 blends leading to a variety of azimuthal combustion instabilities. The influence of the hydrogen content, the air mass flow rate and the equivalence ratio on the instabilities is investigated over a wide range of operating conditions with mean chamber pressures from 1.5 to 3.3 bar. This leads to a range of exit boundary conditions, from partially to fully reflecting. It is found that pure methane and methane-hydrogen mixtures with low hydrogen contents result in stable combustion. However, when the hydrogen content reaches 25% by volume high-amplitude instabilities are excited, which exhibit higher order harmonics with significant pressure amplitude contributions. Such harmonic response was not previously observed in atmospheric annular combustors. The amplitudes decrease slightly when the H_2 content is increased further. The harmonic response is found to be amplitude dependent with fewer significant harmonic contributions occurring at low-amplitudes and a cut-on amplitude of the fundamental mode at which higher harmonics become significant. The interaction between the harmonic components of the pressure amplitudes is shown to follow a quadratic relationship. The modal response was analyzed and it was found that all high-amplitude instabilities feature clockwise spinning modes whereas lower-amplitude instabilities feature counter clockwise spinning modes. Finally, a low- and high-amplitude case were investigated in detail and phase-averaged images are discussed. The low-amplitude instabilities result in flame dynamics similar to those observed in atmospheric combustors previously whereas the high-amplitude instabilities exhibit large oscillations in the flame height and intensity. A characterization of the boundary conditions is also provided for numerical simulations which includes temperature measurements, acoustic characterization and cold flow velocity profiles.

1. Introduction

The shift towards renewable energy sources, such as wind and solar power, is leading to an increasing share of intermittent energy sources in the future energy mix. Gas turbines are seen as a vital enabling technology for renewable energy sources as they are highly dispatchable, meaning they can be rapidly deployed to stabilize the grid [1].

A promising way to reduce carbon emissions is to increase the use of hydrogen as a fuel. While the introduction of hydrogen into the fuel (usually CH_4) can increase the flammability limit and power density, the high reactivity of hydrogen can also promote

flashback [2]. Even a modest addition of hydrogen leads to an increase in the laminar flame speed and a reduction of the flame height which can have a major impact on the thermoacoustic stability of a combustor [3,4].

Thermoacoustic instabilities result from a constructive coupling between the acoustic field and fluctuations in the heat release rate that lead to large pressure oscillations [5], thereby limiting the operational envelope and reducing the life time of the combustor. Despite decades of investigation, self-excited thermoacoustic instabilities still remain a serious problem and further understanding of the phenomenon in practically relevant configurations is needed [6,7].

Modern gas turbines and aeroengines often have annular combustion chambers. Azimuthal modes propagating in either direction around the annulus have been observed in industrial combustors [8–10], and have been reproduced in atmospheric

* Corresponding author.
  E-mail address: thomas.indlekofer@ntnu.no (T. Indlekofer).

pressure laboratory combustors [11–13], as well as high-fidelity numerical simulations [14,15]. Azimuthal modes can take the form of standing modes, with a fixed nodal line position, spinning modes with the nodal line spinning around the annulus at the speed of sound, or a combination of both leading to mixed modes. These modes can undergo continuous transitions between either mode nature [11,12,14,16], a phenomenon commonly referred to as *modal dynamics* [9]. Over the last decade, the dynamic nature of these modes has received significant attention from the scientific community. Modal dynamics were shown to be dominated by the effects of symmetry breaking [11,17–20] and turbulent noise [9,21,22].

Even though several laboratory annular combustion chambers now exist [11,13,23], they usually feature an exit boundary condition open to atmosphere. This complicates the transferability to industrial engines (gas turbines for power generation operate at around 20 bar [24]) and the ability to conduct high fidelity numerical simulations due to complex boundary conditions [6,25]. Subsequently, there is a need for choked experimental rigs, enabling the study of combustion instabilities with more realistic acoustic boundary conditions at higher pressures, turbulence levels and power densities.

There has been a number of studies investigating the dynamics of swirl or bluff body stabilized flames at elevated pressure in single isolated flames. Freitag et al. [26] measured flame transfer functions (FTFs) from $1.1 - 5\ bar$ to investigate the effect of pressure on the FTF. They found that pressure can introduce a phase shift, which has an influence on the stability of a combustor. In terms of the gain, the effect of pressure led to a higher response at higher frequencies and the opposite at low frequencies. This finding was supported by Cheung et al. [27]. Sabatino et al. [28] found that elevated pressure modifies the flame-vortex interactions causing an increase in the gain. It was also found that the effect of pressure on flame interaction was fuel-dependent. While the local maxima of the FTF increased monotonically for methane, for propane it increased until 3 bar and then dropped.

Under well controlled laboratory conditions there are only a few pressurized experiments in annular combustion chambers. Fanaca et al. [29,30] introduced a down-scaled model of an Alstom gas turbine, which was operated at elevated pressure but did not feature self-excited azimuthal instabilities under fully choked exit conditions. Under forced operation, they observed a difference between FTFs of the single sector and annular combustor which was attributed to differences in the resulting aerodynamics. Mazur et al. [31] reported self-excited longitudinal and azimuthal modes in a pressurized annular combustor. However, the occurrence of azimuthal modes was linked to a flashback phenomenon precluding long run times but strong harmonic contributions appeared which were not observed in previous atmospheric studies.

In addition to the effect of pressure on self-excited azimuthal modes, information on the thermal state and acoustic boundary conditions of the combustor is also needed for high-fidelity simulations. Progress depends on both simulations and experiments, and therefore, part of the aim of this research is to provide a test case that can replicate as many of the important boundary conditions found on a real engine as possible, whilst maintaining the well-controlled conditions of an optically accessible lab setup.

This work constitutes the first detailed study of azimuthal combustion instabilities at elevated pressures across a wide range of operating conditions in order to study the modal dynamics, the role of pressure scaling on the response, and to examine in more detail the behaviour of the harmonic contributions. In addition, a thorough characterization of the boundary conditions was performed.

The paper is organized as follows. First, the setup and the operating conditions are introduced. Then the general system response

in terms of the amplitudes and nature of the modes is investigated and analyzed for different hydrogen contents, air flow rate and equivalence ratio. We then focus our investigation on two particular cases, a high- and low-pressure amplitude case, by analyzing their pressure time-series and flame dynamics.

2. Experimental methods

2.1. Intermediate pressure annular (IPA) combustor

A schematic of the combustor is presented in Fig. 1. Premixed fuel-air mixtures are fed into a cylindrical plenum that conditions the flow (through a bed of glass beads in the expansion) before it passes through a 22 mm thick sintered metal plate and is divided between twelve burners. The twelve burners are comprised of tubes that hold the bluff bodies and counter clockwise swirlers (as viewed from above) which are equally spaced around the circumference of the annular combustor. The lower section of the outer wall consists of a quartz glass window enabling optical access for high-speed imaging. The combustion chamber has a length of 168 mm and an inner/outer diameter of $d_i = 128\ mm$ and $d_o = 212\ mm$ respectively. The outer and inner walls, as well as the dump plane are cooled by separate water circuits. The chamber ends with a symmetric contraction (contraction ratio $CR_c = 7$) before the flow is passed through a choking plate ($CR_p = 5$), which further reduces the outer diameter, leading to $CR_{total} = 35$. A second choking plate can be mounted upstream of the plenum expansion.

Further details and a limited set of data with the upper choking plate are presented in A.1 for comparison, an acoustic characterization of the glass bead section, the sintered metal plate and the swirler is found in A.2 and the supplemental material. Details about the pressure drop across the sintered metal plate are presented in A.3 and information about the cooling heat transfer in Appendix D. The complete 3D CAD model is available in the supplemental material.

2.2. Experimental measurements

Dynamic pressure measurements (Kulite XCE-093 sensors, $1.43 \times 10^{-4}\ mVPa^{-1}$) were recorded at five azimuthal positions ($\Theta_{0-4} = 0, 30, 60, 120$ and $240°$) and two longitudinal positions in the injector tube at $z_1 = -81\ mm$ (upper microphone) and $z_2 = -133\ mm$. The signals were acquired at a sampling frequency $f_s = 51.2\ kHz$ and digitized using a 24-bit DAQ system (NI model 9174). Additionally two Danfoss MBS 3000 pressure sensors monitor the mean pressure in the combustion chamber and the plenum.

A high-speed camera (Phantom V2012) with intensifier and UV filter ($\lambda = 310\ nm$, FWHM 10 nm) and a photo multiplier tube (PMT) with the same UV filter are used to capture OH*-chemiluminescence at $\Theta = 30°$.

To determine the temperature of the bluff body, dump plane and inner wall at certain locations, a pyrometer (Optris CT Laser 3MH) was used. An explanation of the procedure and temperatures for two operating conditions are provided in Appendix C.

2.3. Operating conditions and experimental procedure

The operating conditions are described in Table 1. Air mass flow rates ranged from 61.25 to 122.5 gs^{-1} and the fuel was composed of methane (CH_4) with varying quantities of hydrogen (H_2). Air and fuel are combined in a mixing chamber upstream of the plenum. A range of volume fractions $P_V = \dot{V}_{H2}/(\dot{V}_{CH4} + \dot{V}_{H2})$ of $0 - 0.5$, where 0 is no hydrogen and 1 is pure hydrogen, were investigated. This ratio can be translated to the power fraction P_H, resulting in a
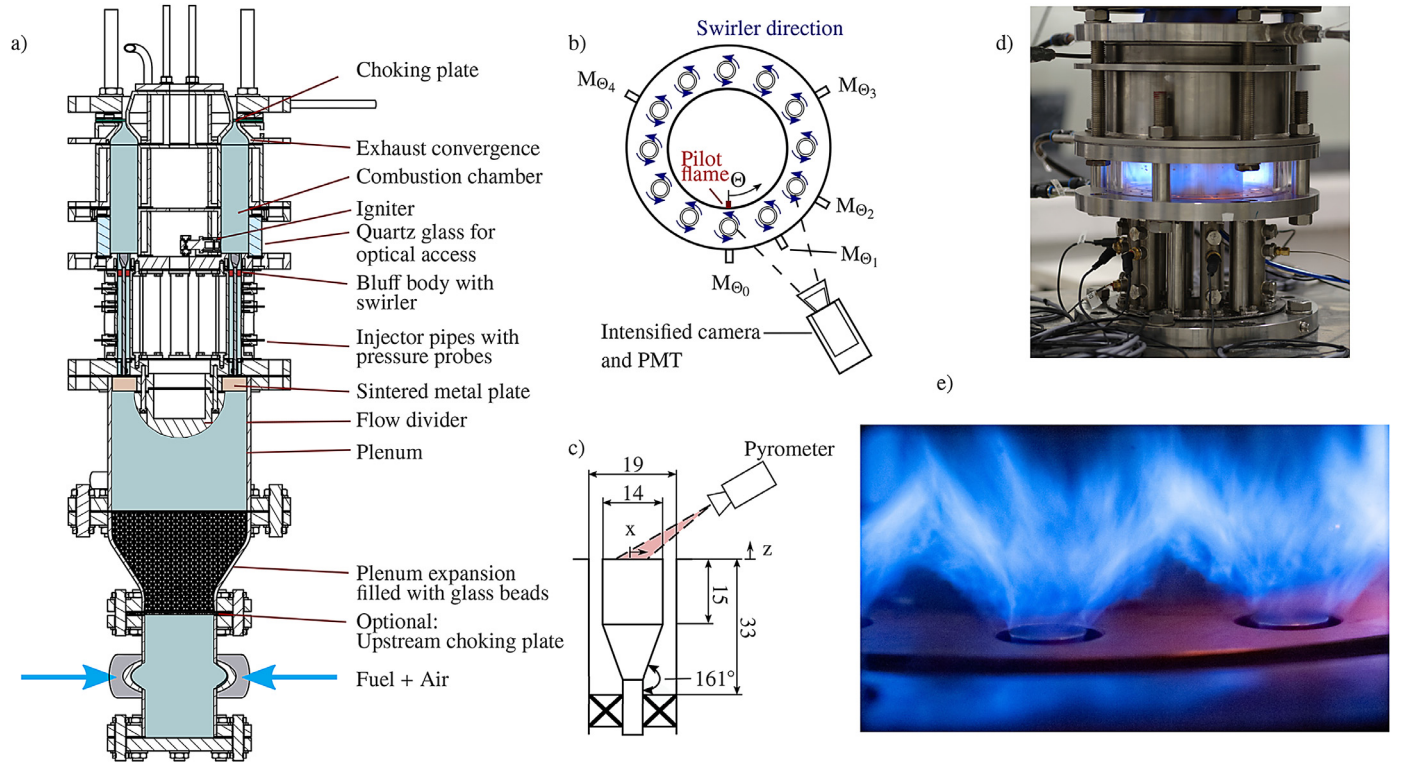
Fig. 1. (a) Schematic of the Intermediate Pressure Annular (IPA) combustor with (b) top view showing the azimuthal position of microphones and the high-speed camera to acquire OH*-chemiluminescence, (c) detailed view of the modified bluff body/swirler assembly (d) Photograph of the IPA combustor during operation and e) quasi-instantaneous image of the flame dynamics.

Table 1
Operating conditions in terms of the air mass flow rate $\dot{m}_a$, the hydrogen power fraction P_H, the hydrogen volume fraction P_V, the equivalence ratio Φ, the laminar flame speed at $p = 2\ bar$ and the resulting thermal power P and exit bulk velocities u_b.

	Stable		Presented data set		Flashback
$\dot{m}_a$ [g/s^{-1}]			61.25–122.5		
P_H	0-0.05	0.1	0.15	0.2	0.25
P_V	0-0.14	0.25	0.35	0.43	0.5
Φ			0.65-1.0		
s_L [m/s^{-1}]		0.17-0.35	0.19-0.39	0.2-0.43	
P [kW]			170-350		
u_b [m/s^{-1}]			28-22		

range of $0 - 0.25$, which was investigated in steps of 0.05. Although stability maps were performed for P_H=0 and 0.05, none of the investigated cases featured self-excited instabilities. For $P_H = 0.25$ it was found that the combustor was prone to flashback. Subsequently, this work will focus on $P_H = 0.1 - 0.2$ with an equivalence ratio (Φ) range of $0.65 - 1$ with steps of 0.05.

Ignition and light-around was performed at $\dot{m}_a = 40.83\ gs^{-1}$, $\Phi = 0.7$ and initiated by a rich ethylene pilot flame at $\Theta = 0°$. This differs from the usual method of ignition in laboratory annular combustion chambers, which typically use one or multiple spark ignitors [32,33]. In the present procedure a combustible mixture is introduced into the combustion chamber only after the pilot flame has been successfully ignited. As soon as a combustible fuel-air mixture reaches the chamber, the pilot ignites a flame kernel which is advected downstream towards the choking plate where it ignites a larger portion of fuel-air mixture and initiates the full light-around which eventually leads to a stabilization of the single flames on the bluff bodies. After successful ignition, the pilot flame is switched off and the flow rates of air and fuel are linearly (constant Φ) increased over 10 s before Φ is increased over 5 s to reach the target operating condition.

2.4. Mode determination

The investigated operating conditions feature self-excited azimuthal modes, which occasionally show significant harmonic components. To separate the different components and harmonic contributions of the azimuthal modes (of order n), the pressure time series are bandpass-filtered with a bandpass width of $\Delta f = 100\ Hz$ centered on the peak frequency f_n.

To determine the nature of the azimuthal modes, the Quaternion formalism, introduced by Ghirardo and Bothien [34] is used. The acoustic pressure in an annulus can be represented as

$$p(\Theta, t) = A \cos(n(\Theta - \theta)) \cos(\chi) \cos(\omega t + \varphi) + A \sin(n(\Theta - \theta)) \sin(\chi) \sin(\omega t + \varphi), \tag{1}$$

with Θ as the azimuthal coordinate and n describing the order of the mode. The orders $n = 1 - 5$ are herein referred to as the fundamental and the first to fourth harmonic frequencies. A describes the amplitude of the mode. The slowly varying real-valued angle $\theta(t)$ describes the angular location of the anti-nodal line and it is bounded between $-\pi$ and π. However, it is important to note that for an increasing order of the azimuthal modes, the number of anti-nodal lines increases. For example for $n = 1$, one anti-nodal line exists, whose position is described by θ or $\theta + \pi$, while a mode of $n = 2$ features two anti-nodal lines whose positions are described by θ or $\theta + \pi/2$. Subsequently, for an unambiguous description, each anti-nodal line position will be described in a range of $[0, \pi/n]$.

The nature angle is described by the slowly varying real-valued angle $\chi(t)$ and indicates whether the azimuthal eigenmode is a standing wave ($\chi = 0$), a pure clockwise (CW) or counterclockwise (CCW) spinning wave ($\chi = \mp\pi/4$) or a mix of both for $0 < |\chi| < \pi/4$. We adopt the reference frame where a CW spinning mode will rotate against Θ and a CCW spinning mode with Θ (see
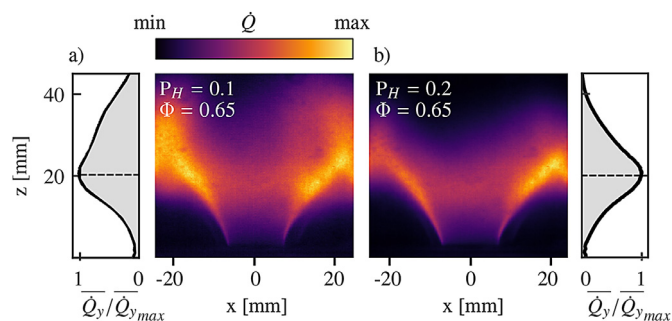
Fig. 2. Mean flame shape and corresponding streamwise distribution of the integrated heat release rate for stable operating conditions: $\dot{m}_a = 91.87 gs^{-1}$, a) P_H=0.1, $\Phi = 0.65$ and b) P_H=0.2, $\Phi = 0.65$.

Fig. 1). The fourth variable φ describes the temporal phase which is related to slow and small changes of the frequency.

3. Experimental results

3.1. General system response and stability maps

Mean flame shapes for two stable operating conditions are shown in Fig. 2 with the streamwise distribution of the integrated heat release rate depicted by grey plots on adjacent sides. Increasing hydrogen enrichment increases the flame temperature, laminar and turbulent flame speeds (see Table 1) and changes the Lewis number (as the diffusivity of hydrogen is high) which generally leads to shorter, more compact flames for the same power [35,36]. In comparison to the previous configuration [31] the flames are more compact and the modified bluff body leads to a wider flame angle with stronger flame-flame interactions at the end of the flame brushes which corresponds to the location of maximum heat release rate.

Although the flame is slightly more compact when $P_H = 0.2$, the location of maximum heat release rate remains at the end of the flame brush. It also reduces interactions with neighbouring flames. This is shown by the much larger interacting region for $P_H = 0.1$ in comparison to $P_H = 0.2$. For the $P_H = 0.1$ case, the flame brushes from adjacent flames can be seen to merge near the side edges of the image. This creates a large vertically oriented region of high heat release rate between the flames found along the sides of the image which extends downstream. This is not observed for the $P_H = 0.2$ flame although there is some evidence of interactions at the flame tips.

Fig. 3 shows the mean chamber pressure $\overline{p}$, bulk velocity u_b, fundamental azimuthal frequency f and the thermal power over a range of Φ for different $\dot{m}_a$ for $P_H = 0.1$. For clarity, data points for all mass flows are only displayed for $P_H = 0.1$, while $P_H = 0.15$ and 0.2 are plotted for $\dot{m}_a = 91.87 gs^{-1}$ only.

With increasing $\dot{m}_a$ and Φ the chamber pressure $\overline{p}$ increases from 1.5 to 3.3 bar. When $\overline{p} > 1.89\ bar$ the choked condition is reached resulting in a fully reflected condition. Therefore cases with $\dot{m}_a > 102.08\ gs^{-1}$ always result in a choked exit condition, while it depends on Φ for lower $\dot{m}_a$. In contrast to $\overline{p}$, u_b decreases with increasing Φ due to the increasing gas temperature and pressure. Nonetheless, increasing $\dot{m}_a$ leads to a slight increase in u_b. The increased flame temperature with hydrogen addition also affects the mean gas temperature in the chamber and thereby the oscillation frequency. The fundamental frequency f lies between $1450 - 1650\ Hz$ and increases with Φ as expected and is relatively insensitive to changes in $\dot{m}_a$ except at the lowest flow rate. At a fixed operating point an increase in P_H results in an increase of P and f whereas $\overline{p}$ and u_b remain almost unaffected noting that only small hydrogen mass fractions were investigated.

During the experiments the combustor exhibited both stable and unstable conditions, including a wide range of instabilities. Figs. 4 and E.6 display the amplitudes normalized by the chamber pressure and the nature angle of the azimuthal modes. Each subplot corresponds to a specific $\dot{m}_a$ and P_H. The color denotes the frequency of the azimuthal mode, e.g. light yellow denotes the fundamental frequency, while purple denotes the fourth harmonic. The normalized amplitude was calculated using the mean value of the Quaternion amplitude at the upper microphone normalized by the chamber pressure. The bar markers show the standard deviation of the time-series for three separate runs (separate test days) illustrating the repeatability of the experiments. A major difference to previous experiments at atmospheric pressures [11,13] is the occurrence of significant higher harmonics for high-amplitude instabilities which will be discussed later in the paper.

Focusing on the general system response first, Fig. 4 shows that the combustor is unstable over large parts of the stability map and stable at lean values of Φ as well as the lowest values of $\dot{m}_a$ for $P_H = 0.1$. With small amounts of hydrogen addition the normalized amplitudes of the fundamental eigenmode reach values that are near the peak values or higher than those found previously in atmospheric annular combustors [11–13]. Peak oscillation amplitudes occur for $P_H = 0.1$ and the largest $\dot{m}_a$. They reach 2% of the chamber pressure which translates to 6 kPa at the upper microphone and 8.5 kPa at the dump plane (evaluated from the multiple microphone method).

In all cases the onset of the instabilities occurs at leaner operating conditions with increasing $\dot{m}_a$. A similar trend is also found for increasing P_H.

Considering the case of $P_H = 0.1$, A increases slightly with $\dot{m}_a$. Just after the onset of the instability, the amplitude of the fundamental mode initially shows a weak but non-monotonic variation with Φ with a consistent dip in the amplitude occurring around $\Phi = 0.85$ after which further increases in Φ result in an increase in A. Overall, the amplitude variation of the higher harmonics also shows similar trends. The only notable difference being a slight decrease in A of the first harmonic for increasing Φ.

For $P_H = 0.15$, the onset of the instabilities occurs at leaner Φ, however the overall trends are similar to those observed for $P_H = 0.1$. Initially the amplitude of the excited fundamental mode is slightly lower compared to the $P_H = 0.1$ case but eventually increases to similar values. The amplitude variation with Φ shows a stronger non-mononotic response and an increasingly pronounced dip in amplitude when $\dot{m}_a > 81.67\ gs^{-1}$. The location of the dip occurs at increasing equivalence ratio as $\dot{m}_a$ is increased and therefore exhibits a Strouhal number dependence (which is not shown directly here for brevity). The amplitude response of the harmonics follows the fundamental component closely. The harmonics only reach a significant amplitude when the amplitude of the fundamental mode is high. This *cut-on* behaviour is described later. It is also worth noting that at this hydrogen power fraction, self-excited instabilities appear for the lowest $\dot{m}_a$ reducing the stability window.

When P_H is increased to 0.2, the amplitudes are significantly lower compared to the previous cases. Only at stoichiometric conditions and lower mass flow rates does the amplitude of the fundamental mode surpass 1%.

While the results are not presented, at $P_H = 0.25$ the amplitudes of the instabilities continued to decrease. However, at this hydrogen power fraction occasional flashback events were observed at high Φ. For low levels of hydrogen addition, $P_H = 0 - 0.05$, the combustor was stable. Based on the large differences in amplitude for differing P_H one can see that the stability of the combustor is strongly affected by hydrogen enrichment and varying trends are observed for each distinct set of P_H cases.
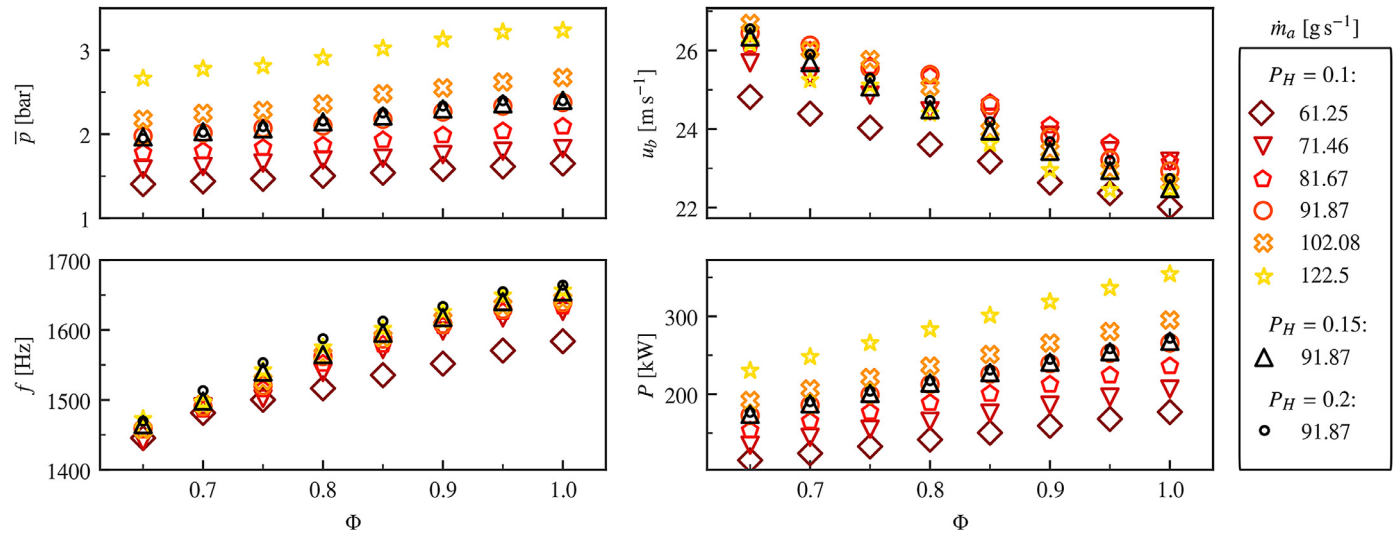
Fig. 3. Mean pressure $\overline{p}$, bulk velocity u_b, fundamental frequency of the azimuthal mode f and thermal power P as functions of $\dot{m}_a$, Φ and P_H.
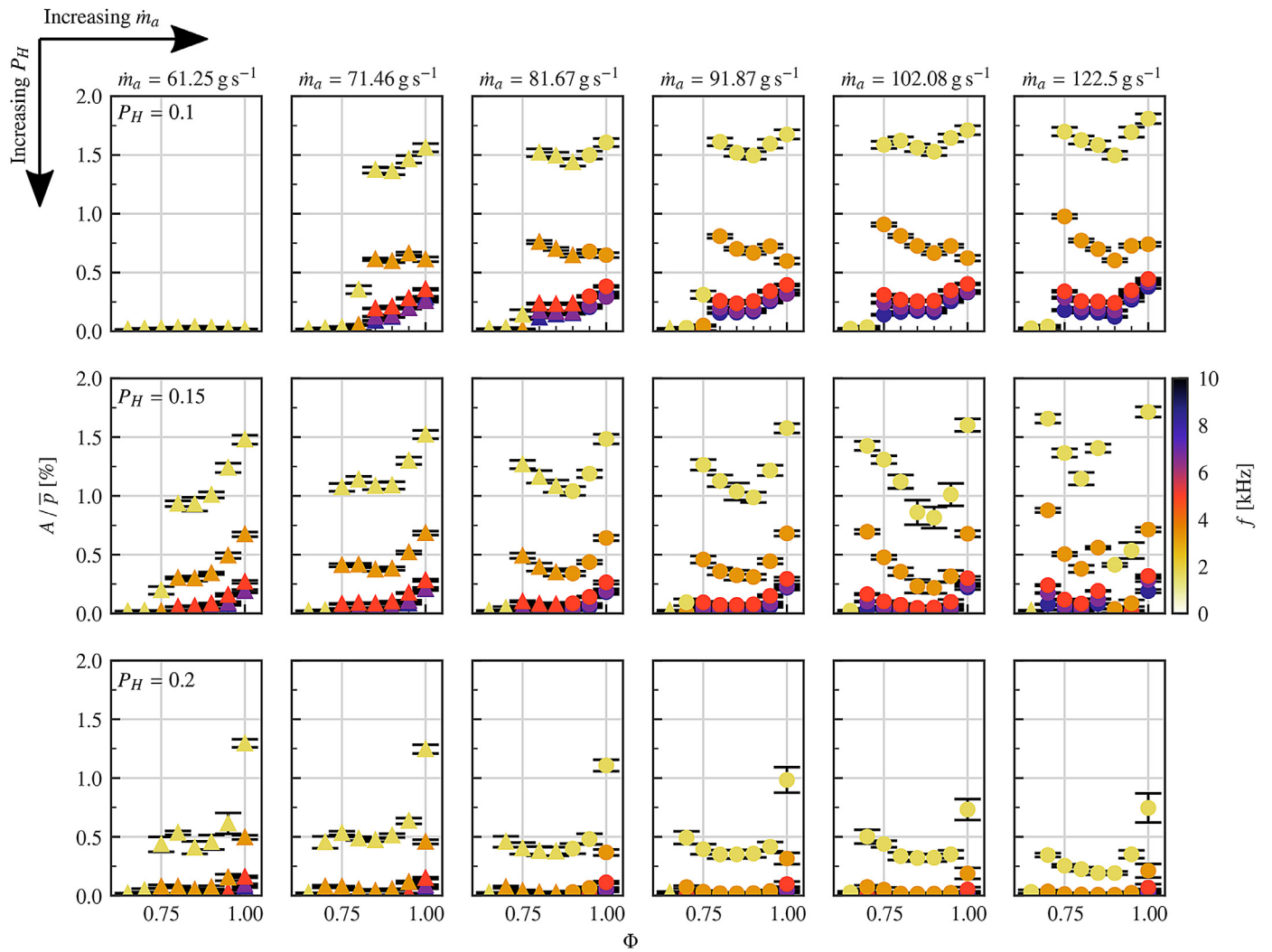

Fig. 4. Mean and standard deviation of the amplitude at the upper microphone for the azimuthal modes (order $n = 1 - 5$) as functions of $\dot{m}_a$, Φ and P_H. Colo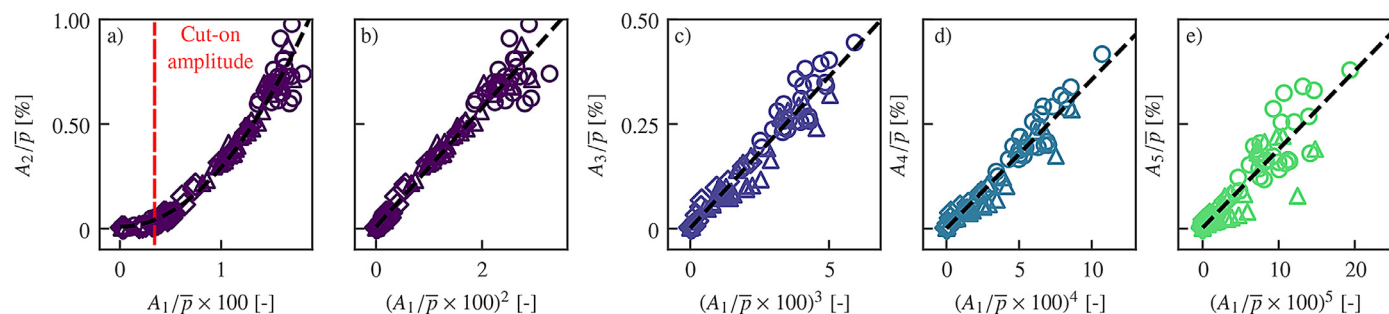r denotes the frequency. Triangular markers correspond to $\overline{p} < 1.89\ bar$, circles to choked conditions at $\overline{p} > 1.89\ bar$.

Fig. 5. Amplitude of the fundamental component $A_{n=1}$ versus amplitudes of the harmonic components $A_{n=2-5}$. Color denotes the order n of the azimuthal component and the marker P_H. Circular markers correspond to $P_H = 0.1$, triangles to $P_H = 0.15$ and diamonds to $P_H = 0.2$. Dashed lines depict the best quadratic (a) and linear (b-e) fits.

Interestingly, the general system response seems not to be altered when the choking condition is fulfilled, for example at approximately $\Phi = 0.9$ and $\dot{m}_a = 81.67 \ gs^{-1}$ for all P_H. A likely reason for this is that the exit nozzle is already strongly reflecting for chamber pressures $> 1.5 \ bar$ [37], thereby when the chamber pressure of 1.89 bar is approached there is not a drastic change in terms of the acoustic boundary condition.

3.2. Harmonic response

The presence of higher harmonics can indicate the presence of nonlinear dynamics. However modelling approaches such as the flame describing function (FDF) do not take them into account based on the assumption that harmonic contributions are small [38]. There are examples where harmonics can contribute significantly to the overall sound pressure level and be included within the FDF framework [39] and given the results presented so far are worth further investigation. The role of harmonics has been investigated previously for single burners under both self-excited [40] and forced conditions [41]. Until now, higher harmonics have not been observed in annular combustors at atmospheric conditions. Under pressurized conditions, their occurrence has been limited to operating conditions with strong intermittent flashback events that were coupled to large-amplitude oscillations [31]. As shown in Fig. 4, in the present work, harmonics corresponding to azimuthal modes of order $n = 2 - 5$ are excited for a wide range of operating conditions.

Fig. 5 plots the relative normalized amplitudes of the harmonics versus the fundamental and shows that there is a correlation between the amplitude of the fundamental and the amplitudes of the higher harmonics. A cut-on amplitude for the first harmonic can be identified in Fig. 5 a), which shows that the amplitude of A_2 only becomes significant when the normalized amplitude of A_1 surpasses $\approx 0.35\%$. Higher cut-on amplitudes were found for the higher harmonic contributions (not shown here). However, this cut-on behaviour cannot be solely due to the large amplitudes as significant harmonics have not been observed in atmospheric experiments with similarly large amplitude instabilities [42]. This strongly suggests that the choked exit conditions play an important role given that the acoustic reflection drops significantly with increasing frequency for an open end [43] in an atmospheric combustor. Similar to [40,41], we observe a quadratic dependence of the amplitudes of the first harmonic on the fundamental component. As shown in Fig. 5 the amplitude of the higher harmonics shows a dependence on the fundamental to the nth power although there is a notable increase in scatter with increasing order.

3.3. Nature angle and modal response

The nature angles of the self-excited modes are plotted in Fig. 6. Only data points exhibiting a normalized amplitude larger than

0.05% are included. In general, the system response near onset conditions leads to CCW spinning modes although there are some cases where standing modes occur. For conditions further away from the stability border the nature angle shows that most of the self-excited modes are strongly spinning in the CW direction over the instability range with the exception of the case where $P_H = 0.15$, $\dot{m}_a = 122.5 \ gs^{-1}$ and $\Phi = 0.85$ which repeatedly features a strong CCW spinning mode with a normalized amplitude of 1.5% (see Fig. 4) and significant harmonics. For cases where $P_H = 0.2$ the nature angle shows that the predominantly CW spinning modes tend more towards mixed modes in comparison to the other cases.

The dynamics observed in these stability maps differ strongly from observations made in the atmospheric version of this combustor [11,12], which has the same dimensions except for the outlet boundary condition and the bluff bodies. In the present work, the spinning modes approach pure spinning modes which have, to date, not been typically found in *noisy* atmospheric annular combustors, which have showed a predominant tendency towards standing modes and mixed modes. A further difference is the suppression of modal dynamics [9], which we define as the instantaneous transitions between standing, spinning and mixed modes. In addition to the change in acoustic boundary conditions, these instabilities have comparably high limit-cycle amplitudes and are subsequently further away from the bifurcation point which may act to prevent instantaneous mode switching due to a larger potential barrier [16] between different attractors. Subsequently, the largest degree of switching and therefore an increased standard deviation, is observed close to the stability borders, while the mode was not observed to change nature as soon as the CW state was reached.

A handful of theoretical papers have tried to shed light on the mode selection in annular combustors [9,20,21,44,45]. Specifically, [45] showed that the ratio of the amplitude to background noise of the combustor is a key parameter that determines the nature of the mode. Thereby an increasing amplitude is expected to excite purer spinning modes. To the best of the authors' knowledge this has not been investigated experimentally. Fig. 7 shows the relation of A and χ on the fundamental and the harmonic components over the full range of operating conditions. Overall, Fig. 7 shows that as the amplitude increases the modes tend towards strongly CW spinning modes for all harmonics. Beginning with the fundamental mode, standing modes appear first at low amplitudes which then quickly transition towards CCW modes as the amplitude increases. At high amplitudes mixed/CW spinning modes become dominant. The occurrence of CCW spinning modes decreases with mode order as almost pure CW spinning states become dominant. This is related to the cut-on amplitudes observed in Fig. 5.

Fig. 7 also shows different behaviour to previous observations made in [31], where the higher order modes could have a different χ and showed a higher probability of standing modes. How-
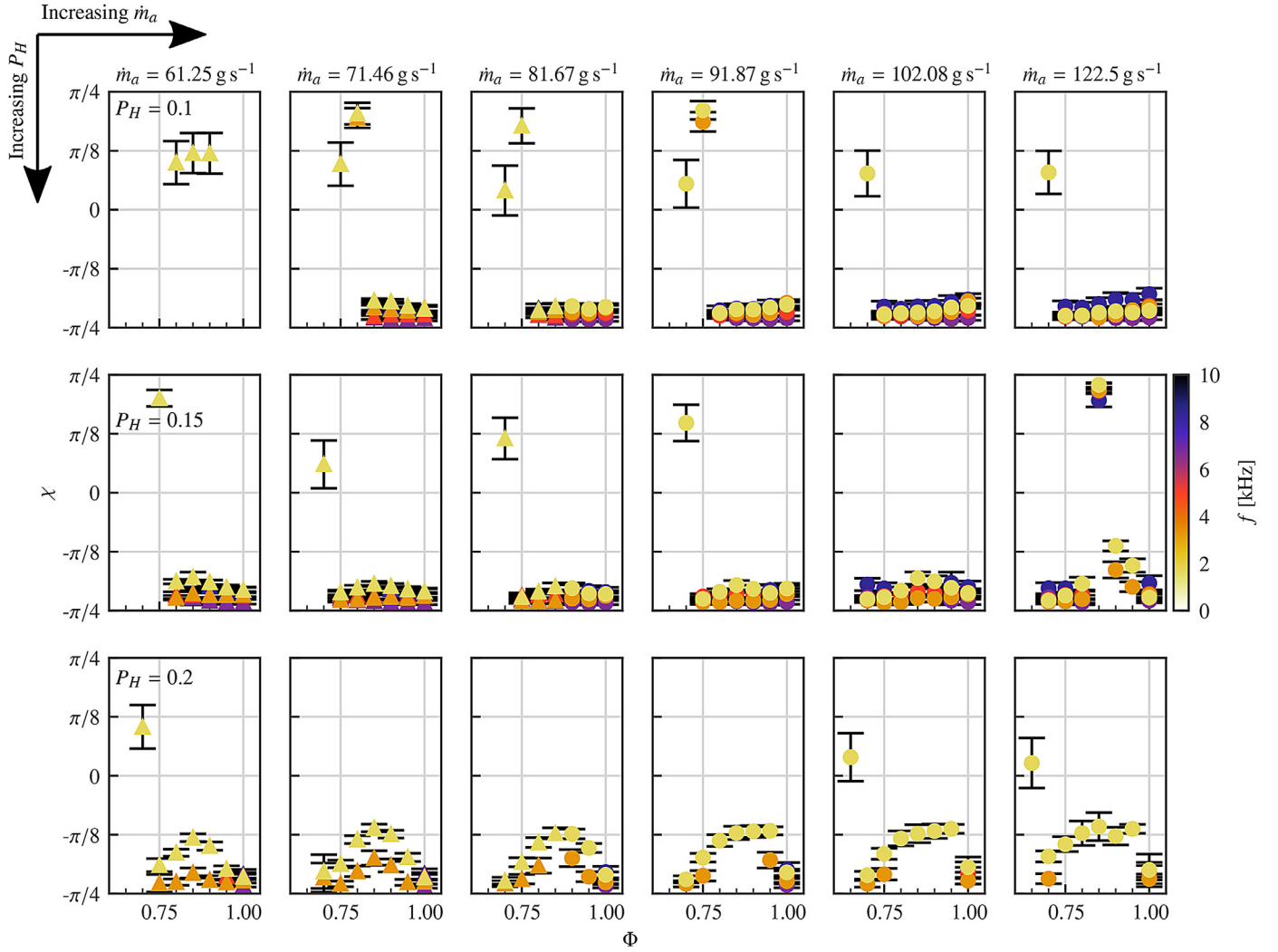
Fig. 6. Mean and standard deviation of the nature angle for the azimuthal modes (order $n = 1 - 5$) as functions of $\dot{m}_a$, Φ and P_H. Color denotes the frequency. Triangular markers correspond to $\bar{p} < 1.89 \, bar$, circles to choked conditions at $\bar{p} > 1.89 \, bar$.
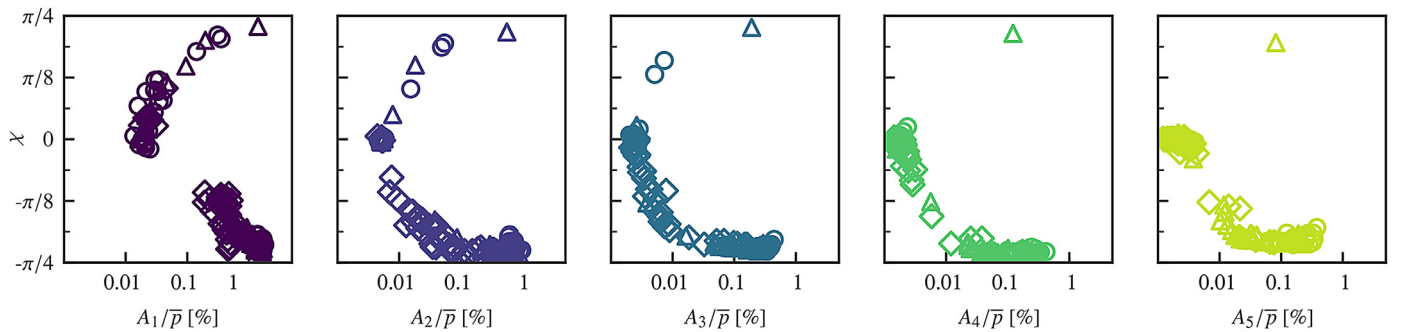

Fig. 7. Nature angle in dependence of the amplitude for the fundamental and harmonic components. Circular markers correspond to $P_H=0.1$, triangles to $P_H=0.15$ and diamonds to $P_H = 0.2$.

ever, that could be attributed to the occurrence of states where not all burners exhibited flashback which introduced a significant asymmetry in the heat release response over the annulus, thereby pushing the mode towards a standing mode [9,21].

Although not shown for brevity, it is worth mentioning that clearly preferred orientation angles for the pressure anti-nodes of the standing component, θ, were observed for each operating condition. While the modes are mostly strongly spinning and the standing component of the mode therefore had a minor amplitude,

a preferred θ is most likely an indicator of small geometrical asymmetries that lead to the anti-nodal line locking into a certain position [18,20]. When the harmonic components also showed a preferred orientation, the preferred nodal line position, θ_n, were not always same. For the cases studied it was often found that θ_1 and θ_2 collapsed, but that the higher harmonics preferred different orientations (see for example Fig. 9). For the $P_H = 0.1$ and 0.15 cases, θ_1 and θ_2 are centered around $20 - 30°$ but for $P_H = 0.2$ the pre-
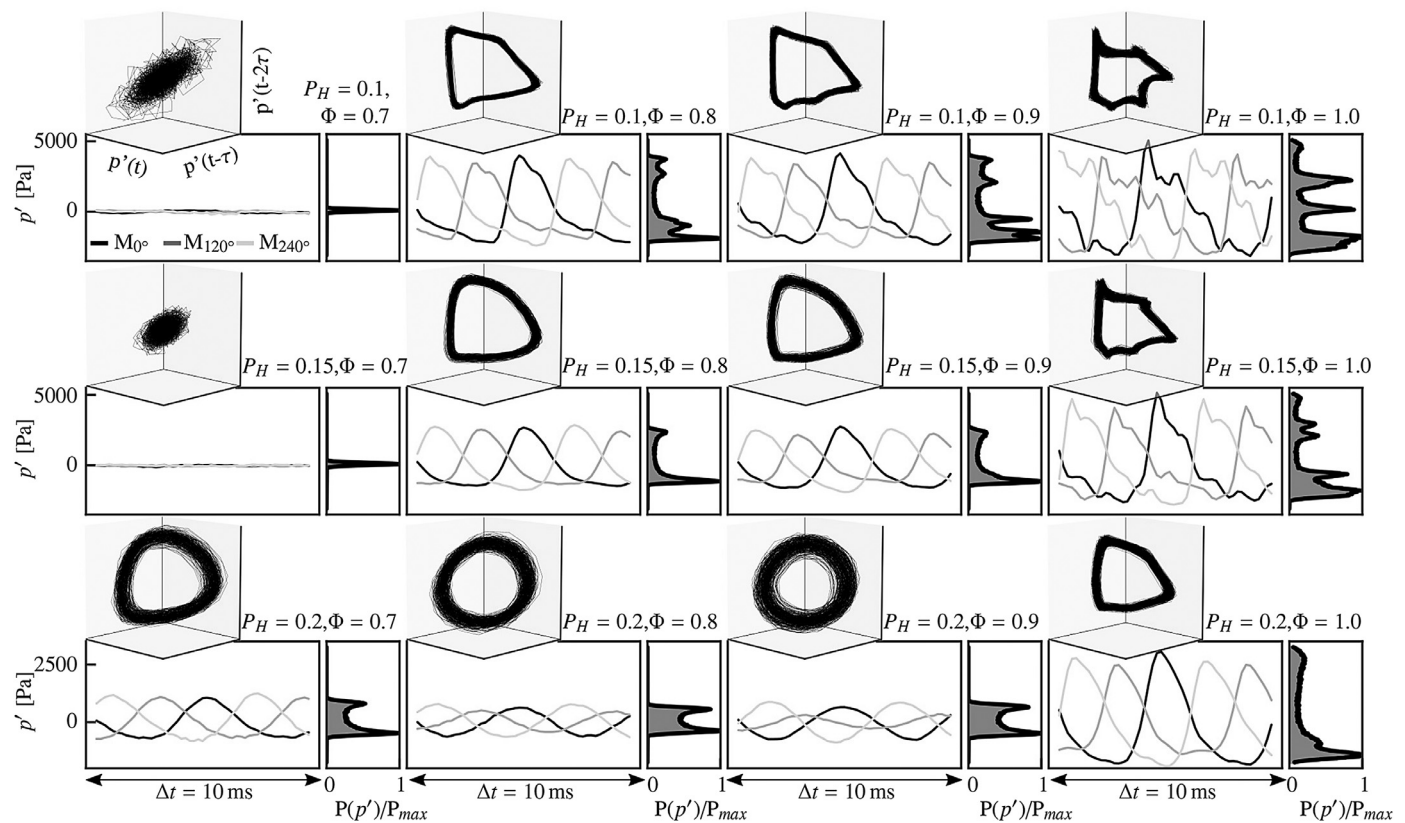
Fig. 8. Time-series, PDFs and phase space plots at $\dot{m}_a = 91.87\ gs^{-1}$ for differing Φ and P_H.

ferred anti-nodal line position transitions quasi-linearly from 60 to 30° for increasing Φ.

3.4. Time series and phase space

Fig. 8 aims to provide a more visual representation of how the harmonic contributions influence the time-series of the pressure fluctuations p'. The plotted data corresponds to $\dot{m}_a = 91.87\ gs^{-1}$ and compares the time-series (with corresponding PDFs) and the phase space plots for $P_H = 0.1 - 0.2$ (shown in rows) for different equivalence ratios, $\Phi = 0.7$, 0.8, 0.9 and 1.0 (shown in columns). The time-series data are cropped to segment lengths of 10 ms while the data used to calculate the PDFs corresponds to a segment of 5 s.

Focusing on the first row, the combustor is initially stable at $\Phi = 0.7$, which is visualized by random trajectories in phase space and the flat response of p'. At $\Phi = 0.8$ the combustor features a strong limit-cycle that has significant harmonic contributions which manifests in a distortion of the phase space and a highly asymmetric PDF which has its mean probability in the region of negative fluctuations. With increasing Φ the peak-to-peak amplitude increases along with the harmonic contribution, leading to a strongly distorted phase space and an increasing number of peaks in the PDF of p'.

As previously discussed, when P_H is increased the amplitude and the degree of harmonic contributions decrease. At $P_H = 0.15$ and $\Phi = 0.8 - 0.9$ the phase space is only slightly distorted resulting in a more sinusoidal response but still features an asymmetry in its PDF. For $\Phi = 1$ the signal is highly distorted with the PDF showing a different distribution compared to the lower hydrogen content case although the amplitude of the fundamental mode is comparable. Still, there is a higher probability of negative p' values, but two smaller peaks occur in the PDF for positive values. The

reason for this is that the amplitudes of the harmonics decrease with order. Higher harmonics are suppressed when $P_H = 0.2$ as is evident in the sinusoidal response in the pressure time-series. At $\Phi = 0.8 - 0.9$ the PDF is symmetric and the phase space shows a uniform torus which again becomes distorted for $\Phi = 1$.

Interestingly, one observes that higher harmonic contributions always lead to a deformation of the acoustic wave, such that the leading edge has a steeper slope than the trailing edge. This phenomenon is known as wave steepening and constitutes a well documented non-linear phenomenon [46].

3.5. Investigation of a high and low-amplitude instability operating condition

In this section we analyze two specific operating conditions more closely: One that features a high-amplitude mode with significant harmonics ($P_H = 0.1$, $\dot{m}_a = 91.87\ gs^{-1}$, $\Phi = 0.8$) and one featuring a low-amplitude instability ($P_H = 0.2$, $\dot{m}_a = 91.87\ gs^{-1}$, $\Phi = 0.8$) with weak harmonics. These cases were chosen as their operating conditions lead to chamber pressures which are high enough to choke the exit nozzle, while the thermal stress is still relatively low, enabling run times that bring the combustor close to thermal equilibrium. Extensive temperature measurements of these two cases are presented in Appendix C.

Fig. 9 shows the time-series, the sound pressure level (SPL) and PDFs of the three slow flow variables A, χ, and θ of the resulting modes.

The ramp procedure for both cases is identical and the onset of the instabilities occurs shortly before the target operating condition is reached. Comparing the SPLs, one can see drastic differences not only in the SPL of the fundamental component, which is more than 10 dB higher for $P_H = 0.1$ but also in the harmonic components which remain significant up to frequencies around 12 kHz.
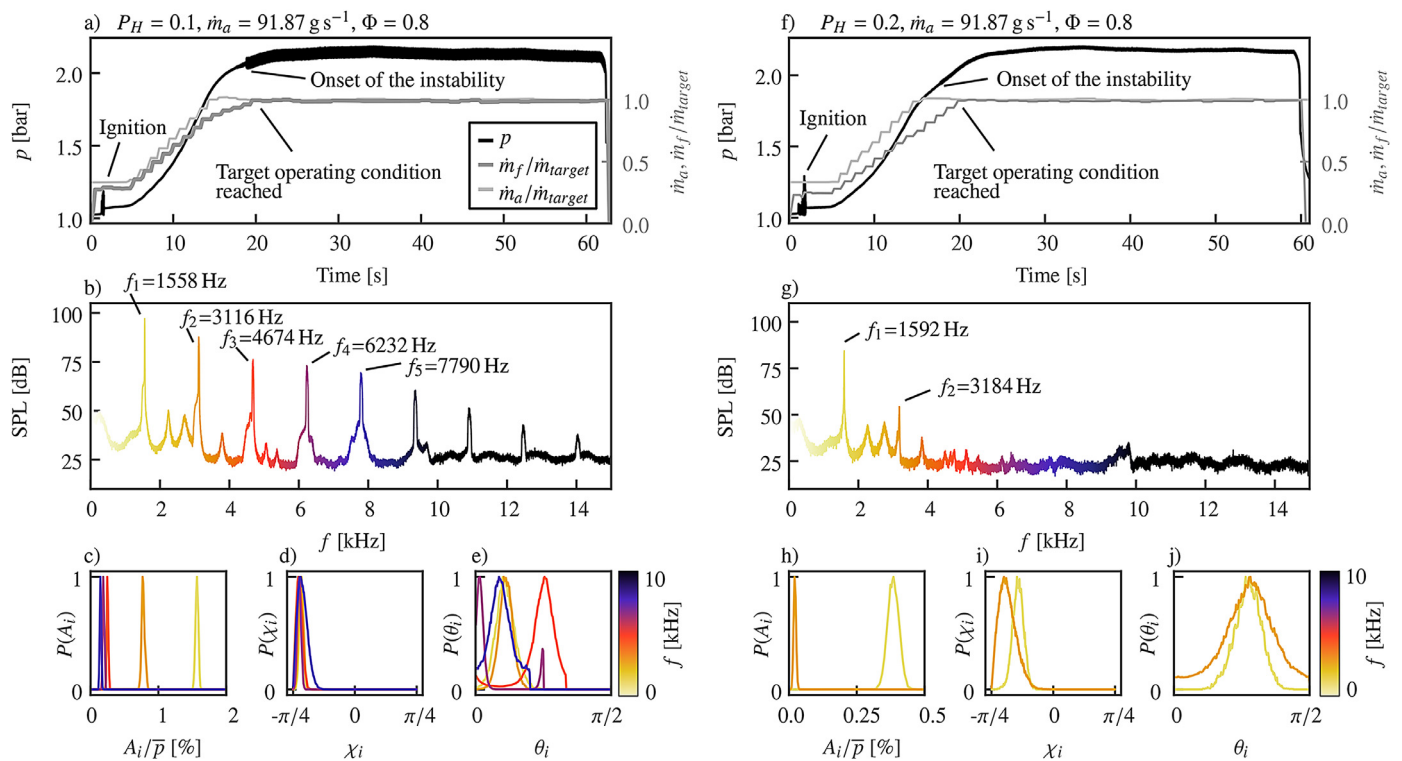
Fig. 9. Pressure time-series, sound pressure level (SPL) and PDFs of the slow flow variables for $P_H = 0.1$ (a-e) and $P_H = 0.2$ (f-j), $\dot{m}_a = 91.87\ gs^{-1}$, $\Phi = 0.8$. The orientation angle θ is displayed from $[0, \pi/2]$ for viewing clarity as no occurrence of $\theta_{n=1} > \pi/2$ was observed.
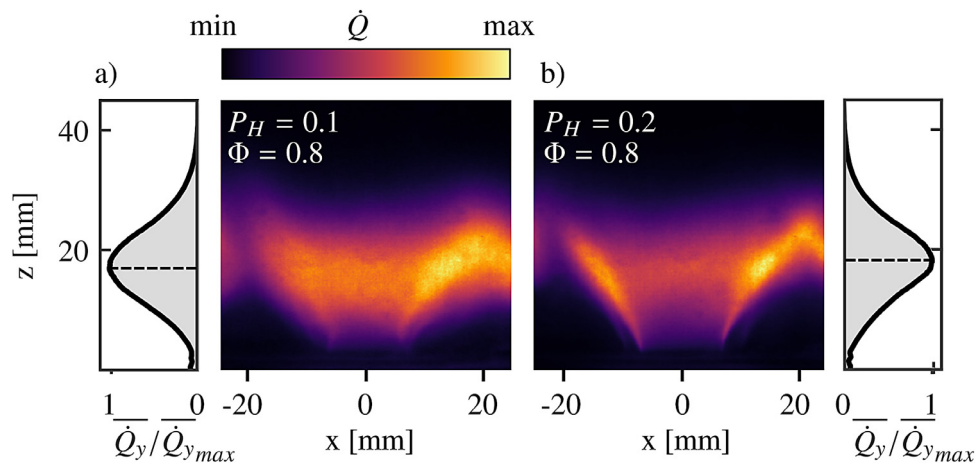

Fig. 10. Mean flame shape and corresponding streamwise distribution of the integrated heat release rate for unstable operating conditions: $\dot{m}_a = 91.87\ gs^{-1}$, a) $P_H = 0.1$, $\Phi = 0.8$ and b) $P_H = 0.2$, $\Phi = 0.8$.

While both cases feature strongly CW spinning modes, χ is closer to a standing/mixed mode for $P_H = 0.2$. No major variability in χ is observed for the fundamental and the harmonic components at $P_H = 0.1$, but the nature angle of the fundamental mode is significantly lower compared to that of the first harmonic for $P_H = 0.2$.

For clarity, θ is displayed from $[0, \pi/2]$ as no occurrence of $\theta_{n=1} > \pi/2$ was observed. Generally, preferred anti-nodal line positions were observed for every n. For $P_H = 0.1$, the preferred θ for $n = 1, 2, 5$ lies at $\approx 20°$ whereas for $n = 3, 4$ it lies at $\approx 0°$ and $45°$ respectively. For $P_H = 0.2$, θ is only shown for $n = 1, 2$ as the amplitudes were very low for the higher harmonics. While the preferred anti-nodal line location for both orders is at $\approx 55°$, this location differs from the locations observed for $P_H = 0.1$.

For comparison to Fig. 2, the mean flame shapes for the investigated cases are shown in Fig. 10. One has to note that despite the

small differences in flame speed and temperature due to the different hydrogen mass fractions, the main difference between the two cases is the amplitude of the instability. Therefore any difference observed in the flame dynamics of the two cases is most likely related to the amplitude of the oscillation (and therefore only indirectly to P_H). During the instability, a drastic change in flame shape occurs for both cases leading to more compact flames. While the stable flames exhibit a slight asymmetry, this asymmetry is increased for the unstable flames leading to a stronger mean heat release rate on the right side of the flame. This may also be related to the effect of the spinning direction of the acoustic mode on the fluctuating heat release rate [47].

To investigate the flame dynamics of both cases, the phase-averaged responses are shown in Fig. 11. For the low-amplitude case (bottom row) flame shapes similar to the stable flames are
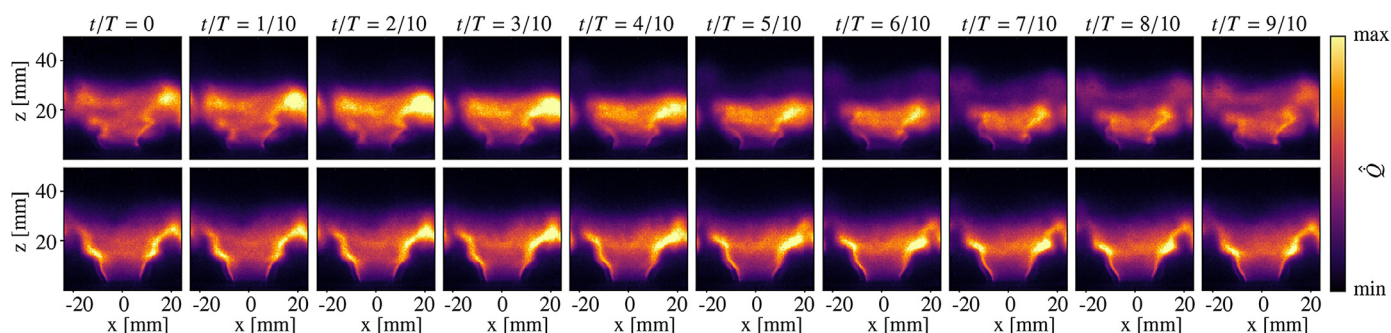
Fig. 11. Phase averaged images for $\dot{m}_a = 91.87\ gs^{-1}$ at $\Phi = 0.8$ and $P_H = 0.1$ corresponding to a high amplitude case (top row) and 0.2 corresponding to a low amplitude case (bottom row). Large modulations to the flame height and intensity are observed compared to the low-amplitude flame dynamics in the bottom row which shows the flame deformed by structures but not affecting the flame height. To calculate the phase averages, the images were divided in 20 bins based on the phase of the fundamental frequency which resulted in more than 300 images per bin.

observed and the flame height shows minimal variation over the cycle. In response to the velocity oscillations at the inlet, the shear layers roll-up leading to the formation of vortex structures which are advected downstream along the flame as can be seen by the modulations along the flame. The presence of such vortex structures is inferred, as these structures roll-up the flame, resulting in observable wrinkles in the phase average distribution. In the case of purely longitudinal velocity oscillations, distortions due to vortex-flame interactions would be axisymmetric. However, these azimuthal instabilties result in both longitudinal and azimuthal velocity oscillations, resulting in an asymmetric response, as shown by the side-to-side flapping motion. This asymmetry can be seen as a slight stagger between the wrinkles on either side of the flame. The flame roll up is also observed to be stronger on the right hand side ($t/T = 1/10 - 4/10$) which is likely the reason for the increased asymmetry in Fig. 10. This suppression of the shear layer disturbance on one side of the flame depending on the spinning direction was previously observed at atmospheric conditions in [47].

Much stronger modulations to the flame shape including a more pronounced asymmetric response appear for the high-amplitude case. This results in much stronger variation of the fluctuating heat release rate. The large pressure amplitudes manifest in strong axial and transverse motions of the flame which strongly distort the flame shape. The stronger transverse flapping motion at the base of the flame, are an indication of stronger azimuthal velocity oscillations. The resulting flame dynamics give rise to a region of peak heat-release rate on the right side of the flame where the interaction with the neighboring flame occurs.

4. Conclusion

The present work introduces an annular combustion chamber operating at elevated pressures and exhibiting self-excited combustion instabilities for a wide range of operating conditions. The largest amplitude self-excited response was found for a hydrogen content of 25% by volume while the amplitudes decreased for larger hydrogen contents. The amplitude of the instabilities showed a non-monotonic dependency on the chamber pressure (which is controlled by the air mass flow rate). While the amplitude tended to increase slightly with increasing pressure for 25% and 35% hydrogen, it decreased slightly for 43%. For all blends amplitude dips were observed at intermediate equivalence ratios. When the combustor featured a high-amplitude instability, significant harmonic contributions are observed, distinguishing these instabilities clearly from recent results in atmospheric combustors. Complex interactions between the fundamental and harmonic components were observed and a quadratic dependence between the amplitude of

a harmonic contribution and the respective lower order contribution was identified. The investigation into the harmonic contributions also revealed a cut-on amplitude at which harmonic contributions become significant. In terms of the nature of the modes, the combustor preferentially exhibited CCW spinning modes close to the stability borders, while all other modes were spinning CW. Fundamental and harmonic components were shown to have differing nature angles. These differences increased for low-amplitude instabilities. For the first time a clear trend between the amplitude and the nature of the azimuthal mode was observed, supporting recent theoretical studies [45] which predicted high-amplitude modes to be spinning while decreased amplitudes push the modes towards standing states. Time-series revealed the distortion of the pressure signals due to harmonic components which results in the leading edge of the pressure signal having a very steep slope during high-amplitude instabilities. Analysis of the flame dynamics also demonstrated the presence of significant asymmetry in the response during both low and high-amplitude instabilities, again distinguishing the response to these azimuthal modes. A thorough characterization of the setup is provided, giving a detailed description of the boundary conditions and thereby positioning this study as a possible baseline case for future simulation studies.

Declaration of Competing Interest

The authors declare that they have no known competing financial interests or personal relationships that could have appeared to influence the work reported in this paper.

Appendix A. Boundary conditions

A1. Effect of an additional upstream choking plate in the plenum

To evaluate the influence of the upstream boundary condition, a choking plate, resulting in a fully reflecting boundary condition, was introduced upstream of the glass bead section in the plenum. The choking plate consists of a 10 mm thick steel plate with 25 holes of diameter 2.2 mm. The investigated set of operating conditions is limited to $\dot{m}_a = 71.46\ gs^{-1}$. Amplitudes and nature angles

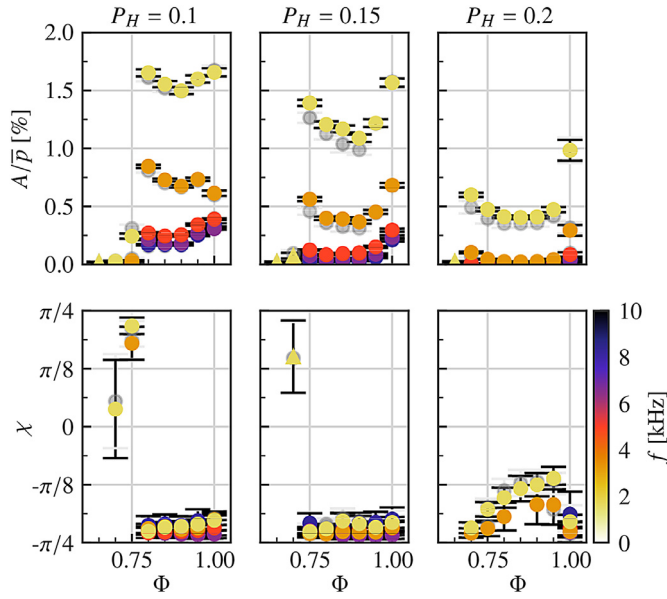Fig. A1. Comparison of three data sets at $\dot{m}_a = 91.87\,gs^{-1}$ with (colored) and without (grey symbols) upstream choking plate.

are displayed in Fig. A1 and compared to the results without upstream choking plate (grey symbols).

Generally, few differences between the two configurations are observed. For $P_H = 0.1$ the normalized amplitudes collapse while A is slightly lower compared to cases without choking plate for $P_H = 0.15$ and 0.2. The onsets of the instabilities are identical and the nature angles show great comparability. In conclusion, the introduction of the upper choking plate does not alter the stability of the combustor in the investigated set of operating conditions. A likely reason for this is the large reflection coefficient of the sintered metal plate which effectively isolates the combustion chamber from the plenum.

A2. Acoustic characterization

Boundary conditions constitute crucial parameters for models aiming to predict the stability of a combustor. Subsequently the acoustic characterization of certain elements is essential and will therefore be presented hereafter. The framework of the scattering matrix, which this characterization is based on is well known and constitutes a convenient description to relate the acoustic interaction between two ducts. For details on the method, the interested reader is referred to [48]. In short, the scattering matrix

$$\begin{pmatrix} p_x^- \\ p_y^+ \end{pmatrix} = \begin{pmatrix} S_{11} & S_{12} \\ S_{21} & S_{22} \end{pmatrix} \begin{pmatrix} p_x^+ \\ p_y^- \end{pmatrix} \tag{A.1}$$

which is used to characterize the element, relates the travelling wave amplitudes p^+ and p^- of two ducts x and y.

We use an impedance test rig based on two straight ducts which are equipped with microphones and connected by the investigated element. Speakers on both or one side act as an acoustic source and we use a total of five independent states. The scattering matrices for the sintered metal plate, the swirler and the glass bead section as well as a description of the setup are made available in the supplemental material S1. Figure A2 displays the S_{11} and S_{12} elements (for notation, refer to [48]) of the sintered metal plate's scattering matrix. For a frequency range up to 3kHz, $|S_{11}|$ lies between $0.7-0.8$ thereby describing a strongly reflective boundary which is likely to be the reason that the introduction of an upper choking plate does not alter the stability of the combustor.
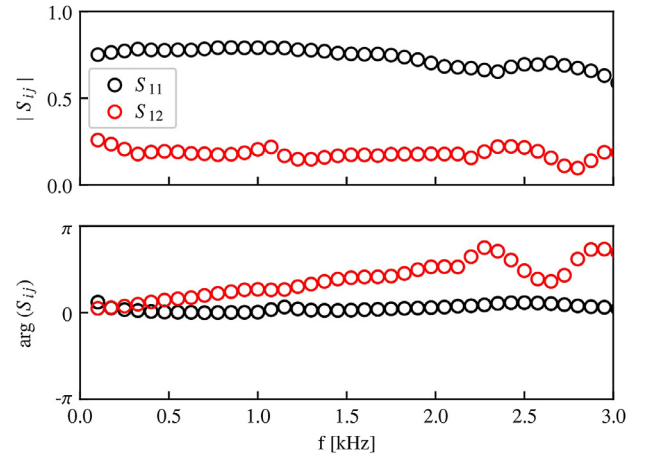

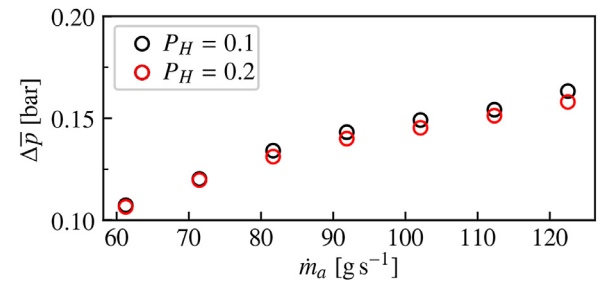
Fig. A2. Scattering matrix of the sintered metal plate.

Fig. A3. Measured pressure drop over the sintered metal plate for $P_H = 0.1$, 0.2 and $\Phi = 0.8$.

A3. Pressure drop over the sintered metal plate

The sintered metal plate (SIKA B-100 from GKN) is made of brass, has a thickness of 22 mm and a porosity of 0.12 at a mean pore size of 183m. Figure A3 displays the measured pressure drop for all air mass flows at $\Phi = 0.8$ and $P_H = 0.1$ and 0.2.

Appendix B. Velocity exit profiles of the injectors

To investigate the exit velocity profiles, as well as the volume flow distribution over the injectors (i.e. the flow asymmetry in the combustor), hot-wire measurements were performed under atmospheric and cold flow conditions. The setup in use is a Dantec Streamline Pro-system equipped with a miniature single wire (55P11) with a probe size of 1.25 mm. The profile was measured 2 mm downstream of the dump plane and the probe was orientated both parallel and perpendicular to the traversing direction. The investigated flow rate is $\dot{m}_a = 91.87\,gs^{-1}$ and the measurements were performed in atmospheric conditions. Figure A4 shows the results for two traversing directions with the probe orientated in parallel. The profile shows a very symmetric pattern. In terms of the flow asymmetry of the full annulus, several injectors were investigated. A comparison of the mass flows calculated based on the measured velocity revealed less than 5% difference between the injectors. This indicates a very symmetric flow distribution.

Appendix C. Temperature measurements

The temperature measurements were performed with an Optris CT Laser 3MH infrared thermometer (spectral range 2.3m, temperature range 0–600°C and response time 2 ms). The measuring spot has a size of 4.5–8 mm depending on the measured location.

As the IR thermometer cannot measure temperatures through flames, the burner has to be switched off to read object temper-
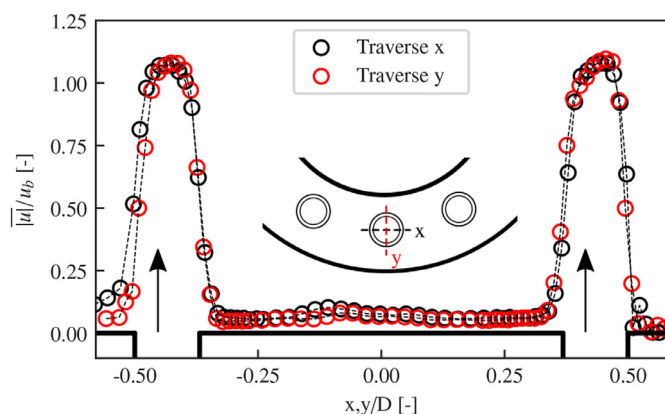
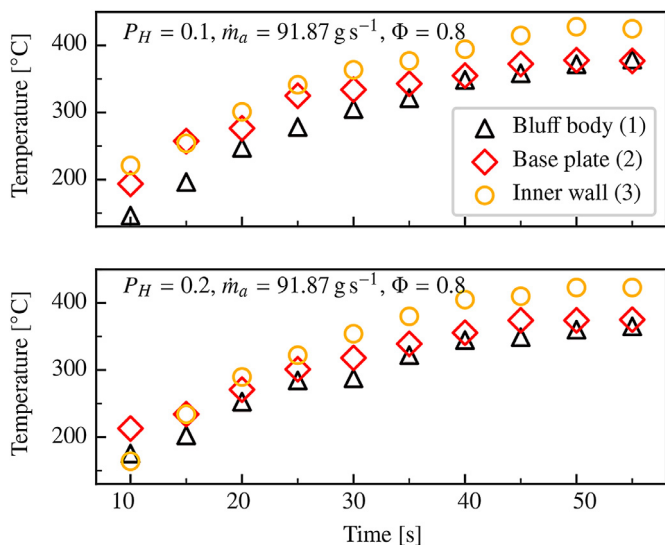Fig. A4. Velocity profile in x and y direction for one injector.

Fig. A5. Temperature T_1-T_3 corresponding to temperatures measured at the bluff body, base plate and inner wall for differing H_2 content.
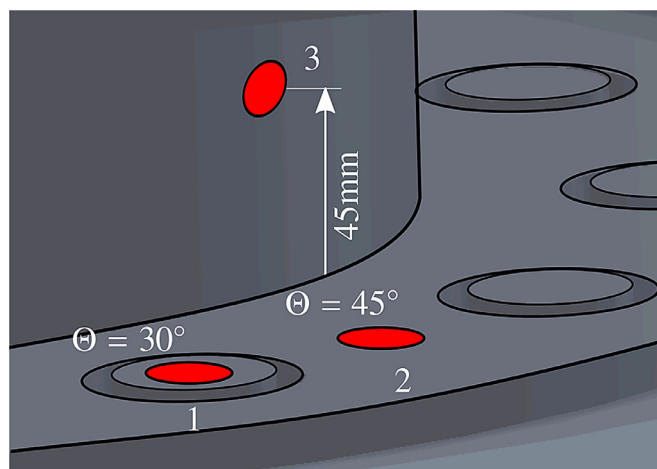

Fig. A6. Detailed view of the combustion chamber showing the measuring positions of the temperatures. Red circle depicts measuring spot.

Table D.2
Volume flow rates $\dot{V}$, inlet and outlet temperatures T_{in}, T_{out} and heat transfer P_{cool} for $\dot{m}_a = 91.87\ gs^{-1}$ at $\Phi = 0.8$ and $P_H = 0.1$ and $P_H = 0.2$.

	Circuit	$\dot{V}$ [L min^{-1}]	T_{in} [°C]	T_{out} [°C]	P_{cool} [kW]
P_H=0.1	Inner	32.9	8.1	55.6	109
	Outer	28.2	8.1	35	52.9
	Back	15.3	8.1	22.9	15.8
P_H=0.2	Inner	33	8	57.2	113.2
	Outer	28.1	8	35.2	53.3
	Back	15	8	22.8	13

ing on the condition the combustor is operated at, the outlet water temperature and thereby the heat transfer over the walls can vary significantly. For brevity, we will limit the information on the two operating conditions which were investigated in detail. The respective information can be found in Table D.2.

Appendix E

Supplementary material

Supplementary material associated with this article can be found, in the online version, at doi:10.1016/j.combustflame.2021.02.015.

References

[1] M.A. Gonzalez-Salazar, T. Kirsten, L. Prchlik, Review of the operational flexibility and emissions of gas- and coal-fired power plants in a future with growing renewables, Renew. Sustain. Energy Rev. 82 (2018) 1497–1513.
[2] M.R. Bothien, A. Ciani, J.P. Wood, G. Fruechtel, Toward decarbonized power generation with gas turbines by using sequential combustion for burning hydrogen, J. Eng. Gas Turbines Power 141 (2019) 121013.
[3] F. Halter, C. Chauveau, I. Gokalp, Characterization of the effects of hydrogen addition in premixed methane/air flames, Int. J. Hydrog. Energy 32 (2007) 2585–2592.
[4] E. Æsøy, J.G. Aguilar, S. Wiseman, M.R. Bothien, N.A. Worth, J.R. Dawson, Scaling and prediction of transfer functions in lean premixed h2/CH4-flames, Combust. Flame 215 (2020) 269–282.
[5] L. Rayleigh, The explanation of certain acoustic phenomena, Nature 18 (1878) 319–321.
[6] T. Poinsot, Prediction and control of combustion instabilities in real engines, Proc. Combust. Inst. 36 (2017) 1–28.
[7] B.T. Zinn, T.C. Lieuwen, Combustion Instabilities in Gas Turbine Engines: Operational Experience, Fundamental Mechanisms, and Modeling, The American Institute of Aeronautics and Astronautics, Inc., pp. 1–26.
[8] W. Krebs, P. Flohr, B. Prade, S. Hoffmann, Thermoacoustic stability chart for high intensity gas turbine combustion systems, Combust. Sci. Technol. 174 (2002) 99–128.

atures (see approach of [49]). Subsequently for the full stability map, only the final temperatures of the bluff body were recorded. For the two operating conditions detailed in this work, more detailed measurements were performed at three locations: Bluff body ($\Theta = 30°$), back plane in between two bluff bodies ($\Theta = 45°$) and at the inner wall ($\Theta = 45°$) 45 mm above the dump plane (see Fig. A6).

To retrieve the transients, the temperatures were evaluated after different run-times, starting from the instant when the target air flow rate was reached ($t = 10\ s$). Practically, the combustor was ignited, run for a certain time, switched off and cooled down until a threshold temperature of the bluff body was reached and then ignited again. Figure A5 depicts the mean values of three runs for each run time up to 1m. One notes that the wall and bluff body temperatures start reaching thermal equilibrium after 50 s and lie at temperatures about $350-400°C$.

Appendix D. Water cooling

The water cooling is divided into three cooling circuits: back plate, inner wall and outer wall. The volume flow is measured by Omega FPB1400 paddle wheel meters and adjusted with control valves. For all operating conditions the flows are set to constant values: $\dot{V}_{inner} \approx 33\ Lmin^{-1}$, $\dot{V}_{outer} \approx 28\ Lmin^{-1}$, $\dot{V}_{back} \approx 15\ Lmin^{-1}$. The inlet water temperature fluctuates between 8-10°C. Depend-

[9] N. Noiray, B. Schuermans, On the dynamic nature of azimuthal thermoacoustic modes in annular gas turbine combustion chambers, Proc. R. Soc. A Math. Phys. 469 (2013) 20120535.

[10] J.R. Seume, N. Vortmeyer, W. Krause, J. Hermann, C.-C. Hantschk, P. Zangl, S. Gleis, D. Vortmeyer, A. Orthmann, Application of active combustion instability control to a heavy duty gas turbine, J. Eng. Gas Turbines Power 120 (1998) 721–726.

[11] N.A. Worth, J.R. Dawson, Modal dynamics of self-excited azimuthal instabilities in an annular combustion chamber, Combust. Flame 160 (2013) 2476–2489.

[12] N.A. Worth, J.R. Dawson, Self-excited circumferential instabilities in a model annular gas turbine combustor: global flame dynamics, Proc. Combust. Inst. 34 (2013) 3127–3134.

[13] J.-F. Bourgouin, D. Durox, J.P. Moeck, T. Schuller, S. Candel, Self-sustained instabilities in an annular combustor coupled by azimuthal and longitudinal acoustic modes, Proceedings of the ASME Turbo Expo (2013). Paper No: GT2013–95010

[14] P. Wolf, G. Staffelbach, L.Y. Gicquel, J.-D. Mller, T. Poinsot, Acoustic and large eddy simulation studies of azimuthal modes in annular combustion chambers, Combust. Flame 159 (2012) 3398–3413.

[15] N. Zettervall, N. Worth, M. Mazur, J. Dawson, C. Fureby, Large eddy simulation of CH4-air and c2h4-air combustion in a model annular gas turbine combustor, Proc. Combust. Inst. 37 (4) (2019) 5223–5231.

[16] A. Faure-Beaulieu, T. Indlekofer, J.R. Dawson, N. Noiray, Experiments and low-order modelling of intermittent transitions between clockwise and anticlockwise spinning thermoacoustic modes in annular combustors, Proc. Combust. Inst. (2020), doi:10.1016/j.proci.2020.05.008.

[17] P. Berenbrink, S. Hoffmann, Suppression of dynamic combustion instabilities by passive and active means, Proceedings of the ASME Turbo Expo (2000). Paper No: 2000–GT–0079

[18] M. Bauerheim, P. Salas, F. Nicoud, T. Poinsot, Symmetry breaking of azimuthal thermo-acoustic modes in annular cavities: a theoretical study, J. Fluid Mech. 760 (2014) 431–465.

[19] J.R. Dawson, N.A. Worth, The effect of baffles on self-excited azimuthal modes in an annular combustor, Proc. Combust. Inst. 35 (2015) 3283–3290.

[20] N. Noiray, M. Bothien, B. Schuermans, Investigation of azimuthal staging concepts in annular gas turbines, Combust. Theor. Model. 15 (2011) 585–606.

[21] A. Faure-Beaulieu, N. Noiray, Symmetry breaking of azimuthal waves: slow-flow dynamics on the bloch sphere, Phys. Rev. Fluids 5 (2020) 023201.

[22] J.-F. Bourgouin, D. Durox, J.P. Moeck, T. Schuller, S. Candel, Characterization and modeling of a spinning thermoacoustic instability in an annular combustor equipped with multiple matrix injectors, J. Eng. Gas Turbines Power 137 (2014) 021503.

[23] J.P. Moeck, M. Paul, C.O. Paschereit, Thermoacoustic instabilities in an annular Rijke tube, Proceedings of the ASME Turbo Expo (2010). Paper No: GT2010–23577

[24] M.P. Boyce, Gas Turbine Engineering Handbook, Elsevier, 2012.

[25] M. Bauerheim, F. Nicoud, T. Poinsot, Progress in analytical methods to predict and control azimuthal combustion instability modes in annular chambers, Phys. Fluids 28 (2016) 021303.

[26] E. Freitag, H. Konle, M. Lauer, C. Hirsch, T. Sattelmayer, Pressure influence on the flame transfer function of a premixed swirling flame, Proceedings of the ASME Turbo Expo (2006) Paper No: GT2006–90540.

[27] W.S. Cheung, G.J.M. Sims, R.W. Copplestone, J.R. Tilston, C.W. Wilson, S.R. Stow, A.P. Dowling, Measurement and analysis of flame transfer function in a sector combustor under high pressure conditions, Proceedings of the ASME Turbo Expo (2003). Paper No: GT2003–38219

[28] F.D. Sabatino, T.F. Guiberti, W.R. Boyette, W.L. Roberts, J.P. Moeck, D.A. Lacoste, Effect of pressure on the transfer functions of premixed methane and propane swirl flames, Combust. Flame 193 (2018) 272–282.

[29] D. Fanaca, P.R. Alemela, F. Ettner, C. Hirsch, T. Sattelmayer, B. Schuermans, Determination and comparison of the dynamic characteristics of a perfectly premixed flame in both single and annular combustion chambers, ASME Turbo Expo (2008). Paper No: GT2008–50781

[30] D. Fanaca, P.R. Alemela, C. Hirsch, T. Sattelmayer, Comparison of the flow field of a swirl stabilized premixed burner in an annular and a single burner combustion chamber, J. Eng. Gas Turbines Power 132 (2010) 071502.

[31] M. Mazur, Y.H. Kwah, T. Indlekofer, J.R. Dawson, N.A. Worth, Self-excited longitudinal and azimuthal modes in a pressurised annular combustor, Proc. Combust. Inst. (2020), doi:10.1016/j.proci.2020.05.033.

[32] M. Philip, M. Boileau, R. Vicquelin, E. Riber, T. Schmitt, B. Cuenot, D. Durox, S. Candel, Large eddy simulations of the ignition sequence of an annular multiple-injector combustor, Proc. Combust. Inst. 35 (2015) 3159–3166.

[33] J.-F. Bourgouin, D. Durox, T. Schuller, J. Beaunier, S. Candel, Ignition dynamics of an annular combustor equipped with multiple swirling injectors, Combust. Flame 160 (8) (2013) 1398–1413.

[34] G. Ghirardo, M.R. Bothien, Quaternion structure of azimuthal instabilities, Phys. Rev. Fluids 3 (2018) 113202.

[35] J.-Y. Ren, W. Qin, F. Egolfopoulos, T. Tsotsis, Strain-rate effects on hydrogen-enhanced lean premixed combustion, Combust. Flame 124 (4) (2001) 717–720.

[36] H. Guo, B. Tayebi, C. Galizzi, D. Escudié, Burning rates and surface characteristics of hydrogen-enriched turbulent lean premixed methane–air flames, Int J Hydrog. Energy 35 (20) (2010) 11342–11348.

[37] M. Zahn, M. Betz, M. Schulze, C. Hirsch, T. Sattelmayer, Predicting the influence of damping devices on the stability margin of an annular combustor, Proceedings of the ASME Turbo Expo (2017). Paper No: GT2017–64238

[38] N. Noiray, D. Durox, T. Schuller, S. Candel, A unified framework for nonlinear combustion instability analysis based on the flame describing function, J. Fluid Mech. 615 (2008) 139–167.

[39] M. Haeringer, M. Merk, W. Polifke, Inclusion of higher harmonics in the flame describing function for predicting limit cycles of self-excited combustion instabilities, Proc. Combust. Inst. 37 (4) (2019) 5255–5262.

[40] K.T. Kim, Nonlinear interactions between the fundamental and higher harmonics of self-excited combustion instabilities, Combust. Sci. Technol. 189 (2016) 1091–1106.

[41] B.D. Bellows, Y. Neumeier, T. Lieuwen, Forced response of a swirling, premixed flame to flow disturbances, J. Propuls. Power 22 (5) (2006) 1075–1084.

[42] T. Indlekofer, A. Faure-Beaulieu, N. Noiray, J. Dawson, The effect of dynamic operating conditions on the thermoacoustic response of hydrogen rich flames in an annular combustor, Combust. Flame 223 (2021) 284–294.

[43] R. Munt, Acoustic transmission properties of a jet pipe with subsonic jet flow: I. The cold jet reflection coefficient, J. Sound Vib. 142 (3) (1990) 413–436.

[44] G. Ghirardo, M.P. Juniper, Azimuthal instabilities in annular combustors: standing and spinning modes, Proc. R. Soc. A Math. Phys. 469 (2157) (2013) 20130232.

[45] G. Ghirardo, F. Gant, Averaging of thermoacoustic azimuthal instabilities, J. Sound Vib. 490 (2013) 115732.

[46] B. Enflo, Theory of Nonlinear Acoustics in Fluids, Kluwer Academic Publishers, Dordrecht Boston, 2002.

[47] J.R. Dawson, N.A. Worth, Flame dynamics and unsteady heat release rate of self-excited azimuthal modes in an annular combustor, Combust. Flame 161 (2014) 2565–2578.

[48] M. Åbom, Measurement of the scattering-matrix of acoustical two-ports, Mech. Syst. Signal Process. 5 (1991) 89–104.

[49] Y. Ding, D. Durox, N. Darabiha, T. Schuller, Chemiluminescence of burner-stabilized premixed laminar flames, Combust. Sci. Technol. 191 (2019) 18–42.